Dynamics of Atmospheres and Oceans 70 (2015) 1–11

Contents lists available at ScienceDirect

Dynamics of Atmospheres and Oceans

journal homepage: www.elsevier.com/locate/dynatmoce

Bimodality and regime behavior in atmosphere–ocean interactions during the recent climate change

Bijan Fallah*, Sahar Sodoudi*

Institute of Meteorology, Free University of Berlin, Carl-Heinrich-Becker-Weg 6-10, 12165 Berlin, Germany

ARTICLE INFO

Article history:
Received 30 November 2014
Received in revised form 16 February 2015
Accepted 21 February 2015
Available online 25 February 2015

Keywords:
Isomap
Maximum covariance analysis
Monsoon
Atmosphere–ocean interaction

ABSTRACT

Maximum covariance analysis (MCA) and isometric feature mapping (Isomap) are applied to investigate the spatio-temporal atmosphere–ocean interactions otherwise hidden in observational data for the period of 1979–2010. Despite an established long-term surface warming trend for the whole northern hemisphere, sea surface temperatures (SST) in the East Pacific have remained relatively constant for the period of 2001–2010. Our analysis reveals that SST anomaly probability density function of the leading two Isomap components is bimodal. We conclude that Isomap shows the existence of two distinct regimes in surface ocean temperature, resembling the break and active phases of rainfall over equatorial land areas. These regimes occurred within two separated time windows during the past three decades. Strengthening of trade winds over Pacific was coincident with the cold phase of east equatorial Pacific. This pattern was reversed during the warm phase of east equatorial Pacific. The El Niño event of 1997/1998 happened within the transition mode between these two regimes and may be a trigger for the SST changes in the Pacific. Furthermore, we suggest that Isomap, compared with MCA, provides more information about the behavior and predictability of the inter-seasonal atmosphere–ocean interactions.

1. Introduction

The climate system appears chaotic but is influenced by complex and high-dimensional processes. Reoccurring climatic phenomena can have a large influence on societies, economies and human health, with extreme events potentially leading to crises of some kind. The Asian monsoon region is one of the world's most populated area, and the higher inter-seasonal fluctuations in the Asian monsoon can lead to major disasters such as floods, droughts, crop damage, *etc.* Hannachi and Turner (2013). Such complex phenomena are resulting from the interplay of different lower boundary forcings such as the oceans (Webster et al., 1998).

El Niño events are the most persistent patterns of ocean variability (Cai et al., 2014; Krishna Kumar et al., 2006) with a direct impact on rainfall's levels, duration and distribution. Cai et al. (2014) found the evidence of increasing probability of extreme El Niño events linked to climate change. The El Niño event of 1997/1998 was the strongest on record and climate models did not predict the strength of this rapid event (McPhaden, 1999). The intensity of this El Niño event may have been affected by the interplay of chaotic climate components (*e.g.*, atmosphere, hydrosphere, biosphere, *etc.*). Many studies have

* Corresponding author. Tel.: +49 30 83871181.
E-mail address: bijanf@zedat.fu-berlin.de (B. Fallah).

http://dx.doi.org/10.1016/j.dynatmoce.2015.02.002

investigated the feedback processes between atmosphere and Pacific ocean (Timmermann et al., 1999; Yeh et al., 2009; Collins et al., 2010; Kug et al., 2010).

According to recent Intergovernmental Panel on Climate Change (IPCC, 2013) report, the tropical rainfall enhanced over land areas during the last decade and the drying trend since mid-1970s to 1990s is reversed https://www.ipcc.ch/. The expected warming trend for the period of 1998–2012 was 0.2 °C per decade (IPCC, 2013). However, the observed global averaged warming rate was 0.04 °C per decade for this period and the climate models were unable to reproduce this hiatus. Among the possible factors (*e.g.*, atmospheric aerosols, oceans and sun) which modulate the global temperature change, equatorial Pacific accounts for the most of the hiatus (Meehl et al., 2013). According to England et al. (2014), strengthening of Pacific trade winds has a dominant impact on cooling of Central equatorial Pacific during this period and the global warming trend is likely to resume once again.

It is always a challenging work to identify the most important modes of multidimensional climate data. Dimensionality reduction techniques are recently used to detect the most important components of the data set that represent the most variability: empirical orthogonal function (EOF) analysis (Jolliffe et al., 2002), Multidimensional scaling (MDS) (Cox and Cox, 2008), Isomap (Tenenbaum et al., 2000), independent component analysis (ICA) (Comon, 1994), locally linear embedding (LLE) (Saul and Roweis, 2000), Laplacian eigenmaps (LEM) (Belkin and Niyogi, 2003). Bretheron et al. (1992) suggested several techniques for isolating the leading modes of variability between two data sets.

Previous studies indicate that there is a direct correlation between sea surface temperature anomaly (SSTA) and rainfall changes (Hastenrath and Greishar, 1993; Giannini et al., 2003; Seager et al., 2005; Hoerling et al., 2006; Krishna Kumar et al., 2006; Schubert et al., 2009). MCA can detect coupled linear atmosphere–ocean teleconnection patterns (Rayner et al., 2003; Dai, 2013). According to Tenenbaum et al. (2000), EOF analysis may be able to find a low-dimensional embedding by preserving its variances. However, many observations contain high-dimensional modes that are invisible to a linear classical dimensionality reduction method like EOF analysis. Hannachi and Turner (2013) applied Isomap to sea-level pressure anomalies to investigate the Asian summer monsoon regime behavior. They suggested that the probability density function of Asian summer monsoon is bimodal. Ross et al. (2008) concluded that Isomap presents no additional modes of climate with respect to classical principal component analysis for ENSO dynamics. Turner and Hannachi (2010) suggested further investigations using the nonlinear dimensionality reduction techniques to explain the monsoon variability.

This study investigates the global atmosphere–ocean variations during the recent climate to understand the possible feedback processes. The spatiotemporal patterns of coupled atmosphere–ocean variations are of major importance especially with respect to their relation to monsoon variability under the recent global warming. Using scale-of-the-art analysis tools will improve the understanding of such complex interactions between different components of the climate system (*e.g.*, oceans and atmosphere).

Here, MCA and Isomap are compared to investigate the most important coupled patterns between rainfall and SSTA in the observed climate. Additionally, we discuss the possible dynamics behind such relationships. To reach the highest confidence due to the increased number of observations (date-rich period), we focused on the recent period 1979–2010.

The study approach is based on the analysis of the effect of non-linearity on two different data reduction methods which are described in the next section. Section 3 contributes to the results, focusing on regime behavior in the atmosphere–ocean changes during the observation period. Discussion and conclusions are presented in Section 4.

2. Data and methods

2.1. Observations

We used monthly precipitation from GPCP Version 2.2 Combined Precipitation Data Set (Adler et al., 2003), NOAA Extended Reconstructed SST V3b (Smith and Reynolds, 2003) and 850 hPa wind from NCEP reanalysis (Kalnay et al., 1996). After removing the seasonal cycle from the data, the monthly anomalies are calculated. In addition, seven different monthly climate indices are used from Earth System Research Laboratory http://www.esrl.noaa.gov/psd/data/climateindices/list/ to define the temporal modes of MCA: Niño3.4, Trans-Niño Index (TNI) (Trenberth and Stepaniak, 2001), North Atlantic Oscillations (NAO) (Hurrell, 1995), Atlantic Meridional Mode (AMM) (Chiang and Vimont, 2004), North Tropical Atlantic Index(NTA) (Penland and Matrosova, 1998), Arctic Oscillations (AO) (Higgins et al., 2002), Pacific Decadal Oscillation (PDO) (Zhang et al., 1997). Combined Northern Hemisphere land-surface air and sea-surface water temperature anomalies (NHT) and land-surface air temperature anomalies only (NHTL) from GISS Surface Temperature Analysis (GISTEMP) are also included in our investigation. The two latter are based on the study of Hansen et al. (2010) (http://data.giss.nasa.gov/gistemp/).

2.2. MCA

MCA applies a single value decomposition (SVD) method to identify the coupled variability of the two dataset (here precipitation and SSTA). Bretheron et al. (1992) used this method to compare different climate components (*e.g.*, ocean and atmosphere). The advantage of MCA, compared with coupled EOF analysis, is that this method captures those modes

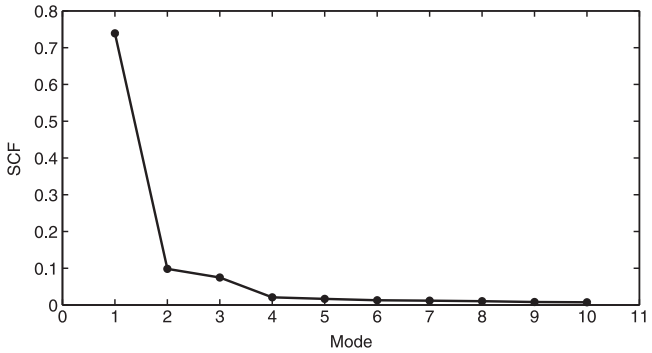

Fig. 1. Squared covariance fraction (SCF) of the first 10 modes of MCA.

of variations which are highly coupled. Thus, the interpretation of the results are easier. First we constructed the cross-covariance matrix of *SST* and precipitation (*P*) for the period of 1979–2010:

$$C = \mathrm{SST}^t P \tag{1}$$

By standardizing *P* and SST we calculated the cross-correlation matrix *C*. Then we calculated the SVD of *C*:

$$C = ALB^t \tag{2}$$

where columns of *A* and *B* are singular values for SSTA and *P* respectively. Temporal expansion of these modes are described as columns of T_A and T_B:

$$T_A = \mathrm{SST}\, A \tag{3}$$

$$T_B = PB \tag{4}$$

and SST = $T_A A^t$ and $P = T_B B^t$ will give the original SST and *P* data. *L* is a diagonal matrix containing the singular values. squared covariance fraction (SCF) is shown by:

$$\mathrm{SCF}_i = \frac{L^2_{(i,i)}}{\sum_{i=1}^{k} L^2_{(i,i)}} \tag{5}$$

2.3. Isomap

The linear methods of dimensionality reduction may fail to capture the correct distance between data-points, if the natural structure of the data is nonlinear. The Isomap algorithm is capable of detecting the nonlinear modes that are hidden in the natural observations (Tenenbaum et al., 2000). The classical dimensionality reduction methods which are used frequently in climate research (*e.g.*, EOF analysis), are based on reconstruction (maintaining the maximum variances) of data set. Isomap applies a classification principal (maximizing the Euclidean distances between samples) (Yang, 2003). The main goal is to find those samples that belong to a lower dimensional manifold that is embedded in an artificially high dimensional data. Here we review the method briefly. The Isomap approach contains three steps: First the Euclidean distances $d_x(i,j)$ between all pairs (i, j) of dataset $(X_{i,j})$ are calculated. Here we did this by considering the *K* nearest neighbors of a reference point. Euclidean distance is an approximation of geodesic distance for the neighboring points. After computing the neighborhood graph, the shortest paths (geodesic distances) following the constructed graph are calculated $(\delta_{i,j})$. The final matrix contains the shortest path distances $(D = \delta_{i,j})$. Finally, the classical Multi-Dimensional Scaling (MDS) is applied to the matrix *D* to extract the principle coordinates and the embedding space.

3. Results

3.1. MCA

The SCF associated with the leading three MCA components are 0.73, 0.10 and 0.07, respectively. Fig. 1 presents a clear elbow at the second MCA mode. However, the differences in the SCF of second and third component are only slightly distinguishable. Therefore, they are inseparable and we considered both modes in our analysis. Figs. 2–4 show MCA patterns of precipitation and SSTA for the period of 1979–2010. We compared the temporal expansions of these modes with several climate indices in order to interpret the temporal evolution of these teleconnection patterns. Table 1 shows the Pearson correlations of these modes with several standard climate indices (ref. Section 2). Correlations only with p−values smaller than 0.01 are shown. The MCA1 of SST has the highest correlations (*corrcoef*. = −0.82) with Niño3.4 index (Fig. 5 and Table 1). The spatial pattern of this mode for SST shows an observed PDO-like pattern. The associated MCA1 pattern of rainfall presents

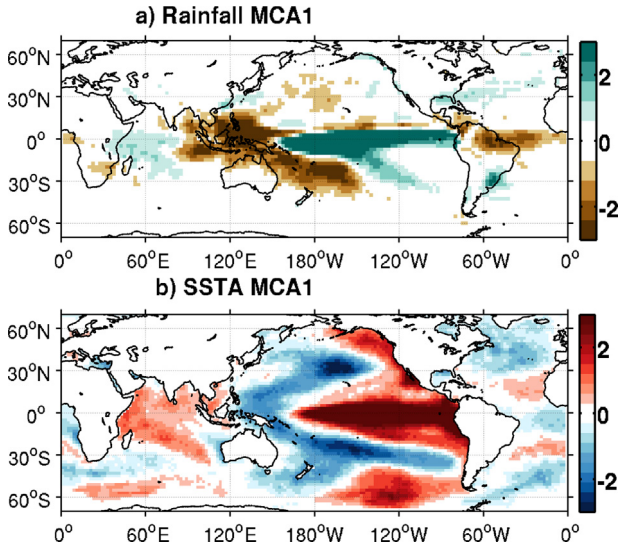

Fig. 2. Spatial patterns of MCA1 for (a) precipitation and (b) SST. (For interpretation of the references to color in this figure legend, the reader is referred to the web version of this article.)

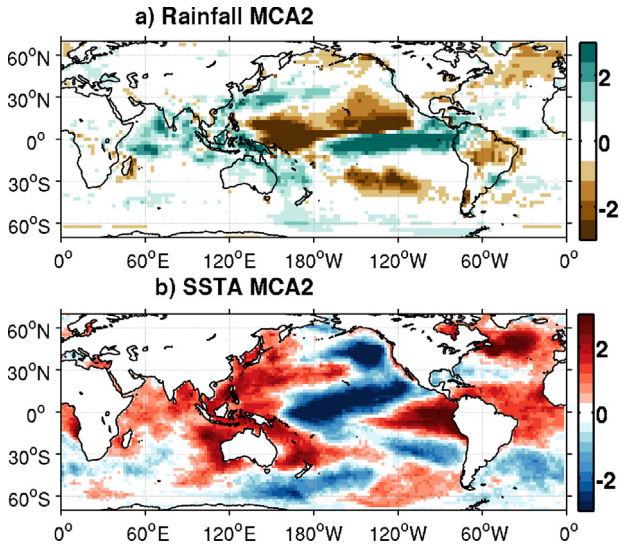

Fig. 3. Spatial patterns of MCA2 for (a) precipitation and (b) SST. (For interpretation of the references to color in this figure legend, the reader is referred to the web version of this article.)

enhanced rainfall over Indonesian Pacific and North Brazil with a decrease over Central Pacific Ocean. The time-series of precipitation for this mode exhibits the highest correlation with Niño3.4 time-series (*corrcoef*. = −0.77). The extreme El Niño of 1997/1998, known as "the climate event of the 20th century" (McPhaden, 1999), is well captured by this mode. MCA2 for SST presents a dipole pattern with the warm Central and cool East Pacific (Fig. 3). Time series of this mode correlates highly with northern hemisphere temperature and TNI (*corrcoef*. = −0.59 and 0.47, respectively). This concludes that El Niño

Table 1
Correlation of MCA modes with climate indices. Bold numbers are the highest correlation in each row. Not significant (NS) indicates correlations with *p*-value > 0.01.

MCA	Niño3.4	TNI	NAO	AMM	NTA	AO	PDO	NHT	NHTL
SST1	**−0.82**	NS	NS	0.19	NS	NS	−0.54	NS	0.15
SST2	NS	0.47	0.17	−0.35	−0.56	NS	0.21	−0.57	**−0.59**
SST3	0.15	0.38	−0.16	0.39	0.57	NS	−0.34	**0.75**	0.73
Precip1	**−0.77**	NS	NS	NS	NS	NS	−0.39	NS	NS
Precip2	NS	**0.62**	NS	−0.18	−0.31	NS	NS	−0.21	−0.22
Precip3	0.2	**0.55**	NS	0.15	0.26	NS	NS	0.45	0.44

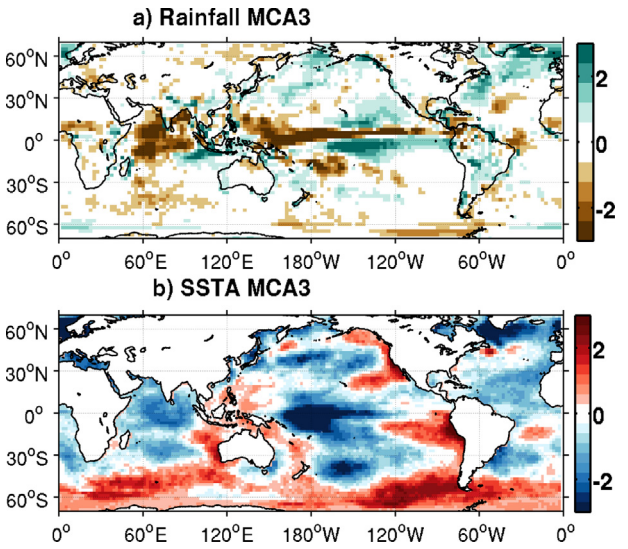

Fig. 4. Spatial patterns of MCA3 for (a) precipitation and (b) SST. (For interpretation of the references to color in this figure legend, the reader is referred to the web version of this article.)

events with the warmer Central Pacific have a greater impact on droughts over India than the East equatorial Pacific. Rainfall pattern of second MCA components also shows a clear precipitation departure over most of the classical monsoon region (Wang et al., 2005) indicating a *break phase* in the monsoon activity.

Temporal expansion of this mode is highly correlated (*corrcoef*.=0.62) with TNI (Fig. 5 and Table 1). As seen in MCA1, MCA2 for rainfall also exhibits a drop in years 1997/1998 coincident with the greatest El Niño event of the 20th century. Fig. 4 illustrates a cool pattern in the equatorial Central Pacific presented by MCA3 of SST which is highly linked (*corrcoef*.=0.75) to northern hemisphere averaged warming (Fig. 5 and Table 1). The best agreement of MCA3 for precipitation is with TNI (*corrcoef*.=0.55) that exhibits wet anomalies over the Western Ghats and northern India (Fig. 5 and Table 1). Thus, the decreasing TNI during the period 2000–2010 (Fig. 5), leads to dry anomalies over the Western Ghats and northern India.

Despite the similar warm pattern in the Central Pacific associated with MCA2 and MCA3, during the extreme El Niño of 1997/1998, the former shows, warm (cool) anomalies over the East (Central) Equatorial Pacific and the latter exhibits no important anomalous pattern. According to MCA3 of SST, an increase in averaged temperature over the northern hemisphere will lead to cooler(warmer) East (central) equatorial Pacific. Within the warming hiatus period of 2001–2010, MCA3 of SST shows cool East equatorial Pacific (Figs. 4 and 5). The coupled rainfall pattern of this mode is linked to negative rainfall departure over monsoon India during this period.

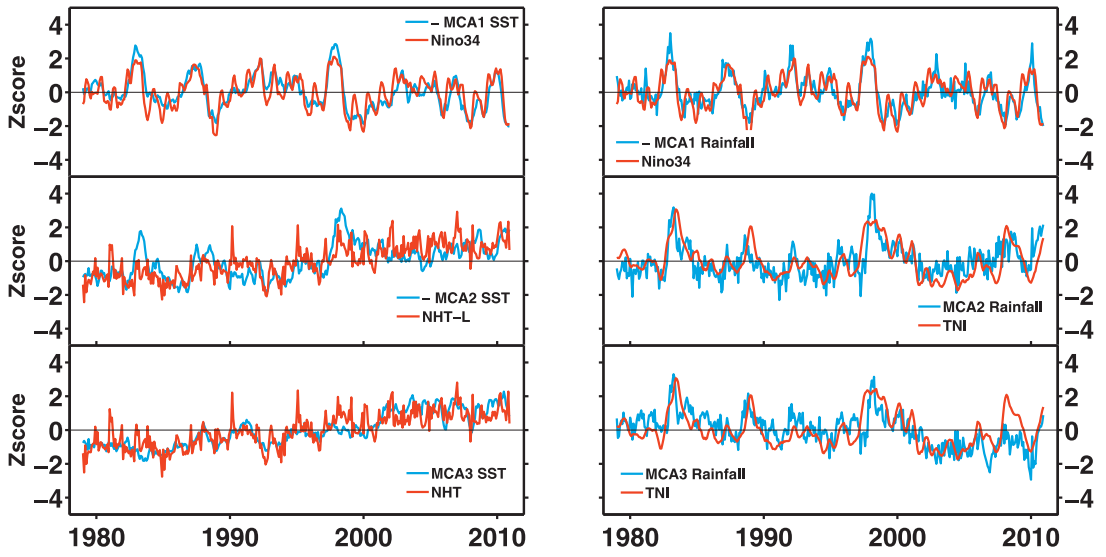

Fig. 5. Time expansions of MCA modes and climate indices with highest correlations (bold numbers from Table 1). Time series have unit-variance and zero-mean. Note that the MCA1 of SST and rainfall as well as MCA2 of SST are multiplied by −1. (For interpretation of the references to color in this figure legend, the reader is referred to the web version of this article.)

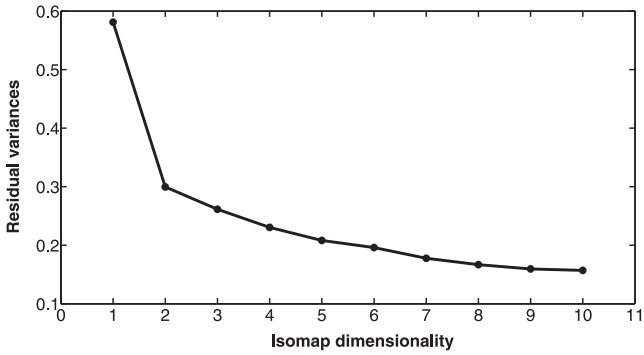

Fig. 6. Residual variance of Isomap vs. dimensionality.

3.2. Isomap

Fig. 6 illustrates the residual variances of Isomap. There is an obvious drop in residual variances at dimension $d = 2$. This indicates that the diversity of the SSTA data has dimension of 2. As in the study of Hannachi and Turner (2013), we focused on the first two Isomap components with 58% and 30% of residual variances. To determine the existence of regime behavior in Isomap components, neighboring graph of the SSTA within the two dimensional embeddings is presented. Fig. 7 clearly suggests two different regime behaviors: prior to 1997 and posterior to 1999. There is a third small cluster of embeddings presented in green circles. This shows the period of extreme El Niño event of 1997/1998. Following the studies of Fallah and Cubasch (2015), Hannachi and Turner (2013, 2013) and Turner and Hannachi (2010), we used Gaussian mixture distribution to estimate the SSTA Probability Density Function (PDF) in Isomap space. The "mixture model" shows the existence of two bivariate Gaussian components. Accordingly, the PDF $F(x)$ can be written as:

$$F(x) = \omega P_1(x) + (1 - \omega)P_2(x) \tag{6}$$

where $\omega = 0.42$ is the mixing proportion of the first and $(1 - \omega) = 0.58$ of the second component. P_i is defined by its mean and covariance. The Expectation Maximization (EM) algorithm is repeated 10,000 times. The transition period of 1997–1998 is excluded when calculating the Gaussian mixture model. Fig. 8 compares the Gaussian kernel PDFs of Isomap and MCA leading two components. Optimal value is used for normal density calculations. Different numbers of K (nearest neighbors) in Isomap exhibit bidimensionality of PDF (not shown). K-Isomap with $K = 12$ is used in this study. Fig. 8 indicates that Isomap shows an obvious bimodality in the leading two modes. In contrast, MCA PDFs are unimodal. PDFs of MCA1 and MCA3 of SSTA also do not depict a clear bimodality (not shown). Fig. 9a illustrates the two-component Gaussian mixture model PDFs

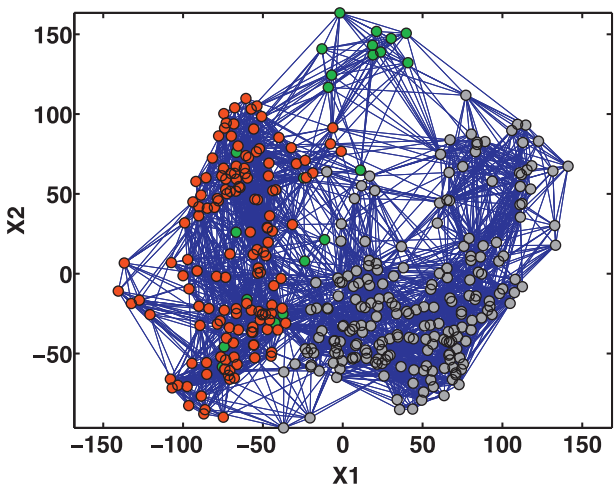

Fig. 7. Two dimensional embeddings of Isomap for SSTA. The gray circles indicate the period of 1979–1996 and the red ones 1999–2010 respectively. The period of 1997–1998 is shown in green circles. (For interpretation of the references to color in this figure legend, the reader is referred to the web version of this article.)

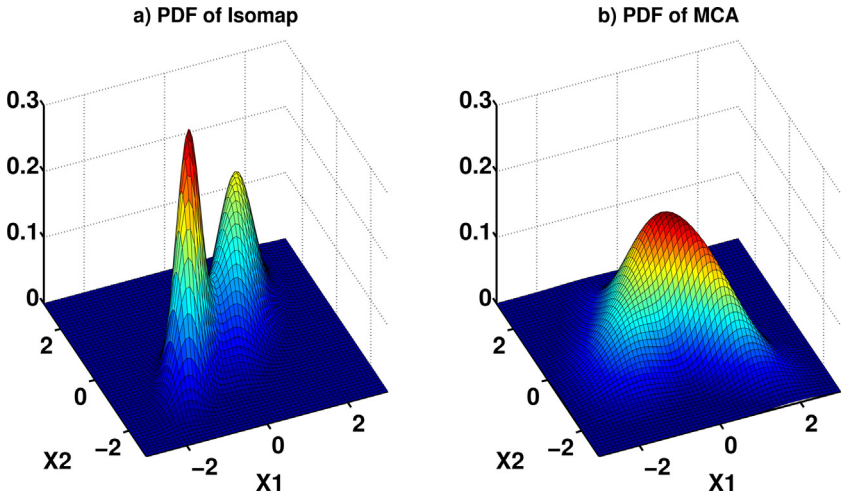

Fig. 8. Gaussian kernel PDFs of leading two (a) Isomap and (b) MCA components.

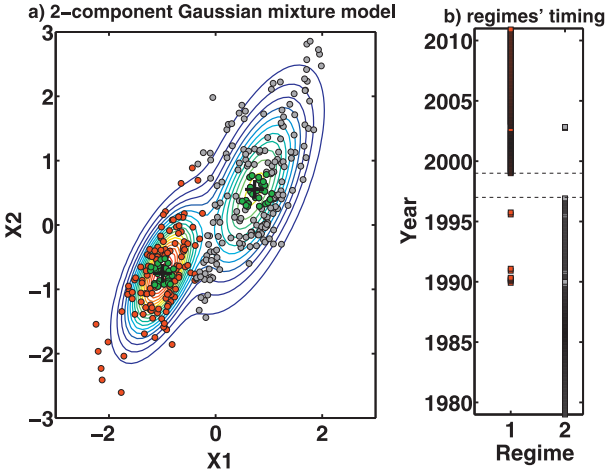

Fig. 9. (a) Two-component mixture model PDFs of two leading Isomap and (b) timing of each component. + indicate the centers of mixture components. Red colors show regime 1 and gray colors regime 2. Green circles indicate 30 nearest months to each center. (For interpretation of the references to color in this figure legend, the reader is referred to the web version of this article.)

of two leading Isomap components. There are two obvious regimes occurring in different time-slices: regime 1 for the period of 1999–2010 and regime 2 for the period of 1979–1996 (Fig. 9b).

Time expansion of Isomap modes of SST and the climate indices with the highest correlations are shown in Fig. 10. Table 2 shows the Pearson correlations between Isomap modes and several climate indices. Isomap1 of SST shows the highest correlation with the Northern temperature anomalies over land surface (*corrcoef*. = −0.75). The second mode of Isomap has significant correlation with PDO time-series (*corrcoef*. =0.51) and the third mode shows significant correlations with North Tropical Atlantic Index (*corrcoef*. =0.42).

We constructed the composites of 30 nearest SSTA and rainfall conditions to these two modes to recognize the atmospheric-ocean conditions associated with the PDFs of Isomap. Fig. 11 illustrates the results of SSTA composites for the two regimes. These patterns were preserved when increasing the number of nearest states. The constructed patterns

Table 2
Correlation of Isomap modes with climate indices. Bold numbers are the highest correlation in each row. Not significant (NS) indicates correlations with *p*-value > 0.01.

Isomap	Niño3.4	TNI	NAO	AMM	NTA	AO	PDO	NHT	NHTL
SST1	0.24	NS	0.18	−0.45	−0.53	NS	0.51	−0.74	**−0.75**
SST2	0.44	0.39	NS	−0.19	NS	NS	**0.51**	−0.17	−0.18
SST3	NS	−0.21	−0.22	0.35	**0.42**	−0.21	0.22	0.15	0.17

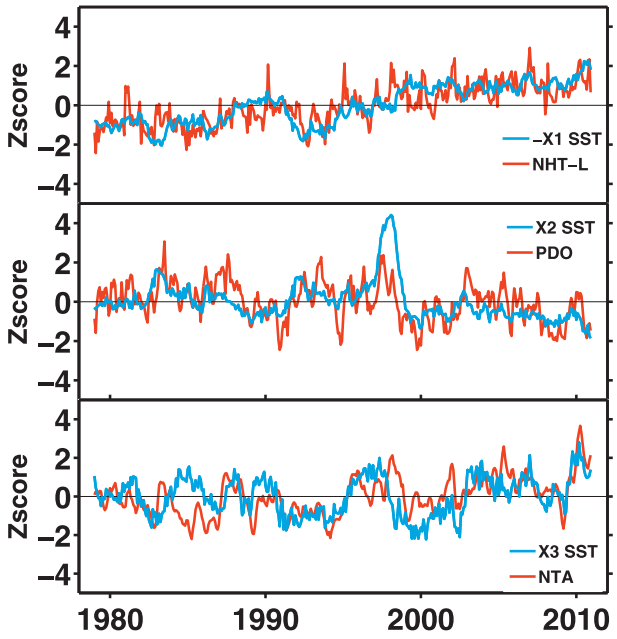

Fig. 10. Time expansions of Isomap modes and climate indices with highest correlations (bold numbers from Table 2). Time series have unit-variance and zero-mean. Note that the X1 of SST is multiplied by −1. (For interpretation of the references to color in this figure legend, the reader is referred to the web version of this article.)

show two particular modes in the ocean conditions. Fig. 11a corresponds to the left-hand PDF center showing generally warmer oceans with a cooler tongue in the Central and East equatorial Pacific (negative PDO), while the right-hand center (Fig. 11b) presents cooler ocean with a warm SST departure in the East Central Pacific Ocean (positive PDO). The associated rainfall anomalies of these two regimes show an increase in equatorial rainfall over land for regime 1 and a clear break phase of rainfall over most of the monsoon areas in regime 2 (Fig. 12). Fig. 13 depicts the 850 hPa large scale circulations associated with SSTA regimes. There is an anticyclonic circulation in the East North Pacific associated with regime 1. This regime also resembles the pronounced strengthening of trade winds over the Pacific. The strengthening of trade winds will push warm water to the West Pacific and increase the upwelling of deep ocean water over eastern equatorial areas.

These results are consistent with the study of England et al. (2014) and Trenberth and Fasullo (2013). Accordingly, the response over monsoon Asia is consistent with the strengthened Somali jet. This pattern will be reversed for regime 2. There is an anomalous weakening of trade winds over West equatorial Pacific in this regime. These distinct results clearly reveal that the climate was shifted to a new regime (negative PDO-like SSTA) after the extreme El Niño event of 1997/1998.

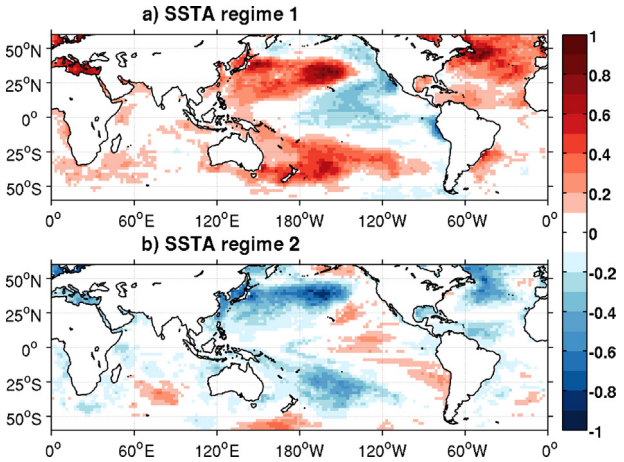

Fig. 11. The composites of SSTA (°C) for 30 nearest months to the PDF peaks of Isomap shown in Fig. 9a: (a) regime 1 and(b) regime 2. (For interpretation of the references to color in this figure legend, the reader is referred to the web version of this article.)

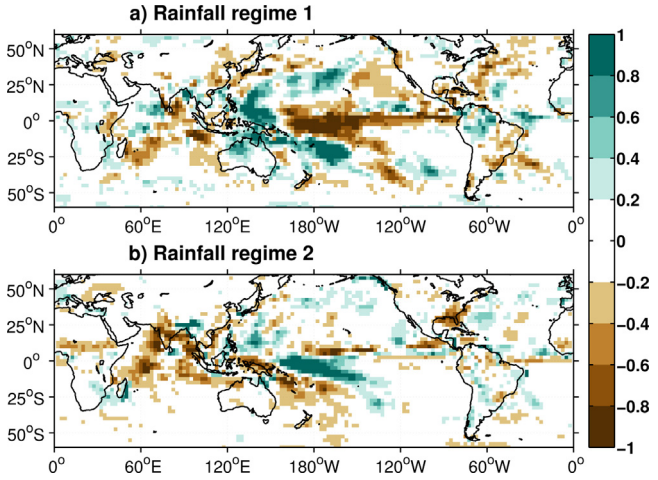

Fig. 12. The composites of rainfall anomaly (mm/day) for 30 nearest months to the PDF peaks shown in Fig. 9a: (a) regime 1 and (b) regime 2. (For interpretation of the references to color in this figure legend, the reader is referred to the web version of this article.)

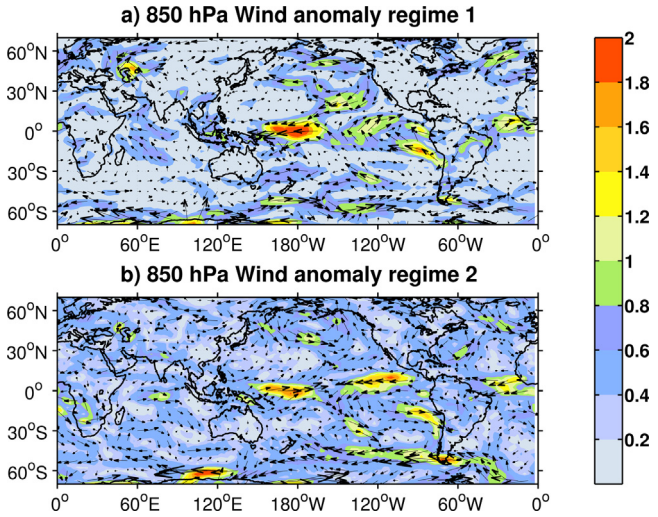

Fig. 13. The composites of 850 hPa wind anomalies for (a) regime 1 and (b) regime 2 from Isomap. Shadings show anomalies of wind magnitude in unit m/s. (For interpretation of the references to color in this figure legend, the reader is referred to the web version of this article.)

4. Discussion and conclusion

In this study we investigated the atmosphere–ocean interactions by using MCA and Isomap analysis of the global rainfall and the SSTA for the period of 1979–2010. In contrast with MCA, Isomap captures more detailed information about the atmosphere–ocean interactions. The bimodality of coupled patterns between the rainfall and SST are clear in the Isomap analysis. The MCA analysis, failed to capture the existence of two different regimes within the recent climate. The results support the study of Hannachi and Turner (2013), who described the advantages of Isomap compared to EOF analysis for inter-seasonal monsoon predictability. The coupled patterns of leading modes of MCA agree well with the study of Krishna Kumar et al. (2006), who concluded that the Central equatorial warmer ("westward-shifted") Pacific Ocean initiates more extreme droughts over India. As an example, no drought occurred in India during the strongest El Niño event of 1997. Time expansions of MCA modes did not show any high correlation with AO or NAO. This indicates that the major variability of coupled patterns may belong to the Pacific Oceans. Our analysis using Isomap also indicates that the particular ENSO event of 1997/1998 did not belong to a typical climate regime. This extreme event occurs within the transition period of the recent climate shift. The first regime presented by Isomap, resembles the cold phase over eastern part of Pacific Ocean (negative PDO) and the second one the warm phase (positive PDO). The former becomes more dominant since 1999, while the latter is more frequent before 1997.

Our results suggest that the strengthened trade winds over the Pacific are coincident with the switch to a cold East equatorial Pacific since 1999. We conclude that regime behavior in SSTA over Pacific is invisible in MCA and interpretations based on such a linear method require further investigations. We explored the linkage between ocean's forcings such as ENSO

and the preferred weather conditions that may improve the inter-seasonal atmosphere–ocean interactions. However, there is still a lack of appropriate observational data and interpretation of results from reanalysis may be misleading. Variations of ocean temperature (*e.g.*, PDO) have alternating cycles of 15–30 years. Climate change investigations may require timescales of more than 50–100 years that is beyond the time-expansion of available observational data. The analysis still suffers from a huge lack of the observational data, especially in deep ocean, assuming that most of the recent heat imbalance is going into the ocean.

Acknowledgments

This study was supported by the BMBF joint research project CADY – Central Asian Climate Dynamics and the university management of Freie Universität Berlin (grant no. 0424262106). We would like to thank Delton Chen for his helpful discussions. We also kindly acknowledge three anonymous reviewers for their thoughtful critiques.

References

Adler, R., Huffman, G., Chang, A., Ferraro, R., Xie, P., Janowiak, J., Rudolf, B., Schneider, U., Curtis, S., Bolvin, D., Gruber, A., Susskind, J., Arkin, P., Nelkin, E., 2003. The version-2 global precipitation climatology project (GPCP) monthly precipitation analysis (1979–present). J. Hydrometeorol. 4, 1147–1167.
Belkin, M., Niyogi, P., 2003. Laplacian eigenmaps for dimensionality reduction and data representation. Neural Comput. 15, 1373–1396.
Bretheron, C.S., Smith, C., Wallace, J., 1992. An intercomparison of methods for finding coupled patterns in climate data. J. Clim. 5, 541–560.
Cai, W., Borlace, S., Lengaigne, M., van Rensch, P., Collins, M., Vecchi, G., Timmermann, A., Santoso, A., MJ, M., Wu, L., England, M., Wang, G., Guilyardi, E., F, J., 2014. Increasing frequency of extreme El Nino events due to greenhouse warming. Nat. Clim. Change 4, 111–116.
Chiang, J., Vimont, D., 2004. Analogous pacific and Atlantic meridional modes of tropical atmosphere–ocean variability. J. Clim. 17, 4143–4158.
Collins, M., An, S.-I., Cai, W., Ganachaud, A., Guilyardi, E., Jin, F.-F., Jochum, M., Lengaigne, M., Power, S., Timmermann, A., Vecchi, G., Wittenberg, A., 2010. The impact of global warming on the tropical Pacific Ocean and El Nino. Nat. Geosci. 3, 391–397.
Comon, P., 1994. Independent component analysis, a new concept? Signal Process. 36, 287–314.
Cox, M.A.A., Cox, T.F., 2008. Handbook of Data Visualization, Multidimensional Scaling, Springer Handbooks Computational Statistics. Springer, Berlin, Heidelberg.
Dai, A., 2013. Increasing drought under global warming in observations and models. Nat. Clim. Change 3, 52–58.
England, M., McGregor, S., Spence, P., GA, M., Timmermann, A., Cai, W., Gupta, A., MJ, M., Purich, A., Santoso, A., 2014. Recent intensification of wind-driven circulation in the Pacific and the ongoing warming hiatus. Nat. Clim. Change 4, 222–227.
Fallah, B., Cubasch, U., 2015. A comparison of model simulations of Asian mega-droughts during the past millennium with proxy reconstructions. Clim. Past 11, 253–263.
Giannini, A., Saravanan, R., Chang, P., 2003. Oceanic forcing of Sahel rainfall on interannual to interdecadal time scales. Science 302, 1027–1030.
Hannachi, A., Turner, A.G., 2013. 20th century intraseasonal Asian monsoon dynamics viewed from Isomap. Nonlinear Process. Geophys. 20, 725–741.
Hannachi, A., Turner, A., 2013. Isomap nonlinear dimensionality reduction and bimodality of Asian monsoon convection. Geophys. Res. Lett. 40, 1653–1658.
Hansen, J., Ruedy, R., Sato, M., Lo, K., 2010. Global surface temperature change. Rev. Geophys. 48.
Hastenrath, S., Greishar, L., 1993. Changing predictability of Indian monsoon rainfall anomalies. Proc. Ind. Acad. Sci.: Earth Planet. Sci. 102, 35–47.
Higgins, R., Leetmaa, A., Kousky, V., 2002. Relationships between climate variability and winter temperature extremes in the United States. J. Clim. 15, 1555–1572.
Hoerling, M., Hurrell, J., Eischeid, J., 2006. Mediterranean climate change and Indian Ocean warming. Nuovo Cimento Della Societa Italiana Di Fisica C: Geophys. Space Phys. 29, 99–104, Workshop on Historical Reconstruction of Climate Variability and Change in Mediterranean Regions, Bologna, Italy, October 5–6, 2004.
Hurrell, J.W., 1995. Decadal trends in the north Atlantic oscillation: regional temperatures and precipitation. Science 269, 676–679.
IPCC Climate Change, 2013. The Physical Science Basis, Technical Report. Cambridge University Press.
Jolliffe, I., Uddin, M., Vines, S., 2002. Simplified EOFs – three alternatives to rotation. Clim. Res. 20, 271–279.
Kalnay, E., Kanamitsu, M., Kistler, R., Collins, W., Deaven, D., Gandin, L., Iredell, M., Saha, S., White, G., Woollen, J., Zhu, Y., Leetmaa, A., Reynolds, R., Chelliah, M., Ebisuzaki, W., Higgins, W., Janowiak, J., Mo, K.C., Ropelewski, C., Wang, J., Jenne, R., Joseph, D., 1996. The NCEP/NCAR 40-year reanalysis project. Bull. Am. Meteor. Soc. 77, 437–471.
Krishna Kumar, K., Rajagopalan, B., Hoerling, M., Bates, G., Cane, M., 2006. Unraveling the mystery of Indian monsoon failure during El Nino. Science 314, 115–119.
Kug, J.-S., An, S.-I., Ham, Y.-G., Kang, I.-S., 2010. Changes in El Nino and La Nia teleconnections over North Pacific-America in the global warming simulations. Theor. Appl. Climatol. 100, 275–282.
McPhaden, M., 1999. El Nino – the child prodigy of 1997–98. Nature 398, 559.
Meehl, G.A., Hu, A., Arblaster, J.M., Fasullo, J., Trenberth, K.E., 2013. Externally forced and internally generated decadal climate variability associated with the interdecadal Pacific oscillation. J. Clim. 26, 7298–7310.
Penland, C., Matrosova, L., 1998. Prediction of tropical Atlantic sea surface temperatures using linear inverse modeling. J. Clim. 11, 483–496.
Rayner, N.A., Parker, D.E., Horton, E.B., Folland, C.K., Alexander, L.V., Rowell, D.P., Kent, E.C., Kaplan, A., 2003. Global analyses of sea surface temperature, sea ice, and night marine air temperature since the late nineteenth century. J. Geophys. Res. 108, 4407.
Ross, I., Valdes, P.J., Wiggins, S., 2008. ENSO dynamics in current climate models: an investigation using nonlinear dimensionality reduction. Nonlinear Process. Geophys. 15, 339–363.
Saul, L.K., Roweis, S.T., 2000. An Introduction to Locally Linear Embedding, Technical Report.
Schubert, S., Gutzler, D., Wang, H., Dai, A., Delworth, T., Deser, C., Findell, K., Fu, R., Higgins, W., Hoerling, M., Kirtman, B., Koster, R., Kumar, A., Legler, D., Lettenmaier, D., Lyon, B., Magana, V., Mo, K., Nigam, S., Pegion, P., Phillips, A., Pulwarty, R., Rind, D., Ruiz-Barradas, A., Schemm, J., Seager, R., Stewart, R., Suarez, M., Syktus, J., Ting, M., Wang, C., Weaver, S., Zeng, N., 2009. A US CLIVAR project to assess and compare the responses of global climate models to drought-related SST forcing patterns: overview and results. J. Clim. 22, 5251–5272.
Seager, R., Kushnir, Y., Herweijer, C., Naik, N., Velez, J., 2005. Modeling of tropical forcing of persistent droughts and pluvials over western North America: 1856–2000. J. Clim. 18, 4065–4088.
Smith, T., Reynolds, R., 2003. Extended reconstruction of global sea surface temperatures based on COADS data (1854–1997). J. Clim. 16, 1495–1510.
Tenenbaum, J., de Silva, V., Langford, J., 2000. A global geometric framework for nonlinear dimensionality reduction. Science 290, 2319–2323.
Timmermann, A., Latif, M., Grotzner, A., Voss, R., 1999. Modes of climate variability as simulated by a coupled general circulation model. Part I: ENSO-like climate variability and its low-frequency modulation. Clim. Dyn. 15, 605–618.
Trenberth, K.E., Fasullo, J.T., 2013. An apparent hiatus in global warming? Earth's Future 1, 19–32.
Trenberth, K., Stepaniak, D., 2001. Indices of El Nino evolution. J. Clim. 14, 1697–1701.
Turner, A.G., Hannachi, A., 2010. Is there regime behavior in monsoon convection in the late 20th century? Geophys. Res. Lett. 37, L16706.

Wang, P.X., Clemens, S., Beaufort, L., Braconnot, P., Ganssen, G., Jian, Z.M., Kershaw, P., Sarnthein, M., 2005. Evolution and variability of the Asian monsoon system: state of the art and outstanding issues. Quaternary Sci. Rev. 24, 595–629.
Webster, P., Magana, V., Palmer, T., Shukla, J., Tomas, R., Yanai, M., Yasunari, T., Monsoons, 1998. Processes, predictability, and the prospects for prediction. J. Geophys. Res.: Oceans 103, 14451–14510.
Yang, M.-H., 2003. Discriminant isometric mapping for face recognition. In: Crowley, J., Piater, J., Vincze, M., Paletta, L. (Eds.), In: Lecture Notes in Computer Science, vol. 2626. Springer, Berlin, Heidelberg, pp. 470–480.
Yeh, S.-W., Kug, J.-S., Dewitte, B., Kwon, M.-H., Kirtman, B.P., Jin, F.-F., 2009. El Nino in a changing climate. Nature 461, 511-U70.
Zhang, Y., Wallace, J., Battisti, D., 1997. ENSO-like interdecadal variability: 1900–93. J. Clim. 10, 1004–1020.